Mechanochemical modification of LiAlH$_4$ with Fe$_2$O$_3$ - a combined DFT and experimental study

M. Dragojlović*[a], I. Milanović [a,b], A. Gradišek[c], S. Kurko[a,b,], M. Mitrić[a], A. Umićević[a], J. Radaković[a,b], K. Batalović*[a,b]

[a] Department of Nuclear and Plasma Physics, Vinča Institute of Nuclear Sciences – National Institute of the Republic of Serbia, University of Belgrade, P.O. Box 522, 11001 Belgrade, Serbia
[b] Center of Excellence for Hydrogen and Renewable Energy CONVINCE
[c] Jozef Stefan Institute, Jamova cesta 39, 1000 Ljubljana, Slovenia
*Corresponding authors: Milijana Dragojlović savic.r.milijana@gmail.com or msavic@vin.bg.ac.rs, Katarina Batalović kciric@vin.bg.ac.rs

Abstract

LiAlH$_4$ is a promising material for hydrogen storage, having the theoretical gravimetric density of 10.6 wt% H$_2$. In order to decrease the temperature where hydrogen is released, we investigated the catalytic influence of Fe$_2$O$_3$ on LiAlH$_4$ dehydrogenation, as a model case for understanding the effects transition oxide additives have in the catalysis process. Quick mechanochemical synthesis of LiAlH$_4$ + 5wt% Fe$_2$O$_3$ led to the significant decrease of the hydrogen desorption temperature, and desorption of over 7 wt%H$_2$ in the temperature range 143-154°C. Density functional theory (DFT)-based calculations with Tran-Blaha modified Becke-Johnson functional (TBmBJ) address the electronic structure of LiAlH$_4$ and Li$_3$AlH$_6$. ^{57}Fe Mössbauer study shows the change in the oxidational state of iron during hydrogen desorption, while the ^{1}H NMR study reveals the presence of paramagnetic species that affect relaxation. The electron transfer from hydrides is discussed as the proposed mechanism of destabilization of LiAlH$_4$ + 5 wt% Fe$_2$O$_3$.

Key words: LiAlH$_4$, DFT, TPD, hydrogen storage, ^{57}Fe Mössbauer, ^{1}H NMR, Fe$_2$O$_3$

Introduction

Hydrogen is considered as one of the ideal replacements for fossil fuels since it is a pure and powerful energy carrier. However, hydrogen storage remains the technological bottleneck before wider adoption. Special attention is drawn to metal hydrides and complex metal hydrides as storage materials, due to their recyclability, low absorption/desorption temperatures, or optimal kinetics. LiAlH$_4$ is a complex metal hydride that consists of an electropositive Li$^+$ ion and a coordination complex [AlH$_4$]$^-$ in which the hydrogen is covalently bonded. LiAlH$_4$ is a focus of research in the last decade, due to its outstanding properties: high gravimetric and volumetric density and easy synthesis [1]. Its theoretical capacity is 10.6 wt% H$_2$ [2] and 7.9 wt% H$_2$, for the first and the second decomposition stage [3].

Although LiAlH$_4$ has a high storage capacity, one impediment for its wide application is slow desorption kinetics. Destabilization of hydride material (by the introduction of dopants that create

defects in the crystal structure, or by adding or removing charge) is discussed previously as the path of decreasing desorption temperature or enhancing the storage properties of metal hydrides [4], and in particular for LiAlH$_4$ dehydrogenation [5]. Mechanochemical synthesis shows advantages over standard techniques due to environmentally clean (no waste) synthesis, economic benefits reflected in the fast-grinding procedures, and reduction of the particle size. An additional benefit of ball-milling is the increase in the surface area and micro-deformations that appear in the lattice [6]. Ball-milling influences the kinetics and thermodynamics of the hydrogen adsorption/desorption process by decreasing the diffusion length and increasing the speed of diffusion [7]. Kinetics is improved in ball-milled samples [8] [9], and, in addition, prolonged milling time leads to the decomposition of LiAlH$_4$ [10]. Various dopants or alloying compounds improve dehydrogenation kinetics of hydrogen storage materials, i.e. lower dehydrogenation temperature [11] [12]and make LiAlH$_4$ promising for various applications not just in chemistry (used for organic substrates). Previous research indicates that iron and iron oxides favorably influence the dehydrogenation properties of LiAlH$_4$ [13] [14] [15]. Li et al. [15] showed how 30 min. milling with 5wt% of Fe$_2$O$_3$ significantly reduces desorption temperature. It is not clear whether the transition metal dopants decrease the melting point of LiAlH$_4$ that is in the range 150˚C - 170˚ C [12] [10] [16] or they accelerate the ionic transformation of [AlH$_4$]$^{2-}$ into [AlH$_6$]$^{3-}$ that is observed near the melting temperatures [17]. Mixing LiAlH$_4$ with a small amount of other metal oxides (e.g., TiO$_2$, Cr$_2$O$_3$, etc.) also enhances its properties [18] [19] [20] [21], resulting in narrower band gap and faster kinetics that enables hydrogen release at a lower temperature. Mal'tseva and Golovanova [22] discussed the stability of LiAlH$_4$ in an experimental study and concluded that it is in correlative relation with impurities present in the analyzed sample. The introduction of dopants causes the excitation of valence electrons to antibonding states which influences the desorption process [23]. Various studies [24] [25] [26] imply that electronic excitations during the physisorption or chemisorption play an important role. Hamers [27] described that there is a difference between thermal desorption and desorption caused by energetic sources of excitation (incident photons or electrons), which are causing electronic transitions. It has been suggested that these transitions provoke the thermal desorption at the material surface [23]. Electronic structure and stability of LiAlH$_4$ and Li$_3$AlH$_6$ were addressed also by DFT [28] [29]. The open question remains how metal oxides affect the desorption kinetics of LiAlH$_4$.

The aim of the study is to investigate the changes in dehydrogenation properties of LiAlH$_4$ upon

addition of Fe_2O_3 by experimental and theoretical approach. We studied the decomposition properties, local structure and hydrogen dynamics of ball-milled $LiAlH_4$+5wt% Fe_2O_3. Furthermore, we performed the DFT study of $LiAlH_4$ and its decomposition product Li_3AlH_6, as well as the study of the effect of the unit cell charge to approximate the influence of the iron oxide addition. We were not able to find any results in literature for TBmBJ and destabilization study for comparison, beside all our effort.

2. Methodology

2.1. Experimental approach

Mechanochemical synthesis of $LiAlH_4$ + 5wt% Fe_2O_3 was performed in a high-energy ball mill (SPEX 5100 Mixer/Mill) in an argon atmosphere with grinding speed 2500 rpm, that consists of a stainless-steel container with the maximal capacity of 100 mg and one hardened-steel ball. The movement of the ball is confined only to the horizontal plane. The mill container was loaded with 95mg of $LiAlH_4$ (purity 97%, Alfa Aesar, GmbH & Co KG Germany) and 5mg of Fe_2O_3 (catalyst grade, Sigma Aldrich). $LiAlH_4$ decomposition products were determined using X-ray powder diffraction (Euraf FR590, recording conditions: step = 0.05°, step time = 1 s, ambient conditions).

Temperature programmed desorption (TPD) measurements were performed in a custom-made designed apparatus connected with the mass spectrometer (MS) Extorr XT100. Around 3 mg of analyzed powder was placed in a sample holder (quartz tube) inside an electrical furnace. Quartz tube with the sample was evacuated to 1×10^{-7} mbar at room temperature. After 30 min, when constant pressure in the whole system was accomplished, heating up of the sample started. We used linear heating with a ramping of 10 °C/min, from room temperature to 300 °C. Simultaneously, the Evolved Gas Analysis (EGA) signals as partial pressures were collected for 8 different m/z ratios: 1 (H), 2 (H_2), 8 (LiH), 17 (OH), 18 (H_2O), 27 (Al), 28 (N_2), 32 (O_2). Hydrogen content (wt.%) was determined by gravimetrical approach, by measuring the mass of the sample upon heating in a ceramic crucible inside of tubular furnace from RT to 300 °C at a rate of 10 °C/min, with helium flow of 30 cm^3/min.

The [57]Fe-Mössbauer spectra were collected at room temperature in standard transmission geometry in constant acceleration mode using a [57]Co (Rh) source. The spectrometer was calibrated by using the spectrum of natural iron. The Mössbauer spectra were fitted by the Recoil program

[30]. The center shift values (CS) are quoted relative to the natural iron ($CS = 0$). The spectra were analyzed by fitting the quadrupole splitting distributions (QSDs) and hyperfine field distributions (HFDs) to the spectra using the Voigt-based method of Rancourt and Ping [31].

The NMR measurements were carried out using a 2.35 T superconducting magnet (Oxford), with the magnetic field corresponding to the proton Larmor frequency of 100 MHz. Commercial $LiAlH_4$, as well as $LiAlH_4 + 5wt\%$ Fe_2O_3 (milled for 1 and 5 min) were sealed in glass vials under Ar atmosphere to prevent contact with water vapor or oxygen. Proton NMR spectra and spin-lattice relaxation times (T1) were measured in heating run from 80 to 400 K (the temperature limit of the setup) using a standard gas flow cryostat. NMR spectra were obtained using spin echoes. Spin-lattice relaxation times were measured using the saturation recovery pulse sequence.

2.2. Computational details

$LiAlH_4$ crystallizes in a monoclinic system (No. 14), $P2_1/c$ space group. Its crystal structure consists of four formula units per unit cell (24 atoms in a primitive cell), and Al is surrounded by four hydrogen atoms [32]. α-Li_3AlH_6, the decomposition product of $LiAlH_4$, crystallizes in a rhombohedral crystalline system (No. 148), R-3[33] space group. As an initial set of data, experimentally determined lattice parameters and atomic positions were used for both hydrides. Calculations are performed using Quantum Espresso program package [34]and Wien2k program package [35], both based on density functional theory (DFT) [36]. For the pseudopotential approach, the exchange-correlation potential was treated within generalized gradient approximations (GGA) by Perdew – Wang [37], with valence electrons ($Li\ 2s^1$, $Al\ 3s^2\ 3p^1$, $H\ 1s^1$). The plane wave energy cut-off is set to 40 Ry for $LiAlH_4$, Li_3AlH_6, LiH, and Li. The k-point mesh is created by a Monkhorst-Pack scheme [38] using $7 \times 7 \times 7$ points for $LiAlH_4$, Li_3AlH_6, $12 \times 12 \times 12$ for Al, $11 \times 11 \times 11$ for Li and LiH, and $4 \times 4 \times 4$ for H_2.

Full potential linearized augmented plane waves + local orbitals (FPLAPW+lo) approach implemented in Wien2k [35] allowed the introduction of local orbitals (lo) in the basis, improving upon linearization and enabling a consistent treatment of the semi core and valence states in an energy window, maintaining suitable orthogonality. The exchange-correlation potential was treated within GGA by Perdew-Burke-Ernzerhof (GGA-PBE) [39] for exchange-correlation. To overcome the bottleneck problem of standard methods in the assessment of the band gap (as excited state property [40]), calculations were performed under TBmBJ [41] (Tran - Blaha

modified Becke Johnson exchange potential, which includes LDA correlation). Parameters were set as follows: RMT (Al) = 1.75 bohr, RMT (H) = 0.95 bohr, RMT (Li)=1.90 bohr while the magnitude of the vector G in the Fourier expansion is set to 20 bohr^{-1}; $R_{MT}K_{max}$ (LiAlH$_4$) =5, $R_{MT}K_{max}$ (Li$_3$AlH$_6$) =5. The k-points sampling was performed using $7 \times 7 \times 7$ grid for LiAlH$_4$, and Li$_3$AlH$_6$. The energy separating core and valence states was set to 6.0 Ry. Structure geometries were optimized, and relaxed by minimization of charge (until it became less than 0.00001e) and forces (until they became less than 0.0001 Ry/bohr).

3. Results and discussion

3.1. Study of LiAlH$_4$ + 5wt.% Fe$_2$O$_3$

3.1.1. Hydrogen desorption behavior

Desorption properties of LiAlH$_4$ + 5wt.% Fe$_2$O$_3$ were determined using Temperature Programmed Desorption coupled with the mass spectrometer. Comparison between the commercial LiAlH$_4$ and the sample modified with Fe$_2$O$_3$, both subjected to TPD, is presented in figure 1. By comparing the partial pressures of each chemical species during desorption (the m/z ratios of eight compounds were monitored) it is evident that 99% of summary MS signal originates from desorbed hydrogen. Therefore, complete H$_2$ desorption observed in LiAlH$_4$ + 5wt.% Fe$_2$O$_3$ is described with three characteristic dehydrogenation peaks at 143 °C, 153 °C, and 161 °C (see fig.1a). According to these results and by comparing them with literature data [42] we can argue that desorption properties are improved due to the addition of Fe$_2$O$_3$: the starting desorption temperature is lowered from 150 °C for LiAlH$_4$, reported in [42], to 143 °C, while the second desorption peak at 153 °C, is significantly lower than 210 °C reported for unmodified LiAlH$_4$ [12] [42]. The commercial sample also shows lower desorption temperature as compared to literature values [12] [42] and not so evident second desorption peak, and this might be due to the impurities present in the sample [22], as discussed in the section 3.2.2.

An additional effect of milling with Fe$_2$O$_3$ is seen when comparing with the commercial sample, fig.1a. During the ball milling, the jar inevitably heats up (from ball impact to powder) and consequently, the sample receives energy. Thus, lowering of the kinetic barrier for hydrogen desorption, and the sorption acceleration could be due to thermal activation or the existence of

surface layer defects [43] that accelerate hydrogen release towards the particle surface. TPD of LiAlH$_4$ + 5wt.% Fe$_2$O$_3$ shows how the addition of a small amount of Fe$_2$O$_3$ reacts as a catalyst [15] and shifts the peak position towards lower temperatures.
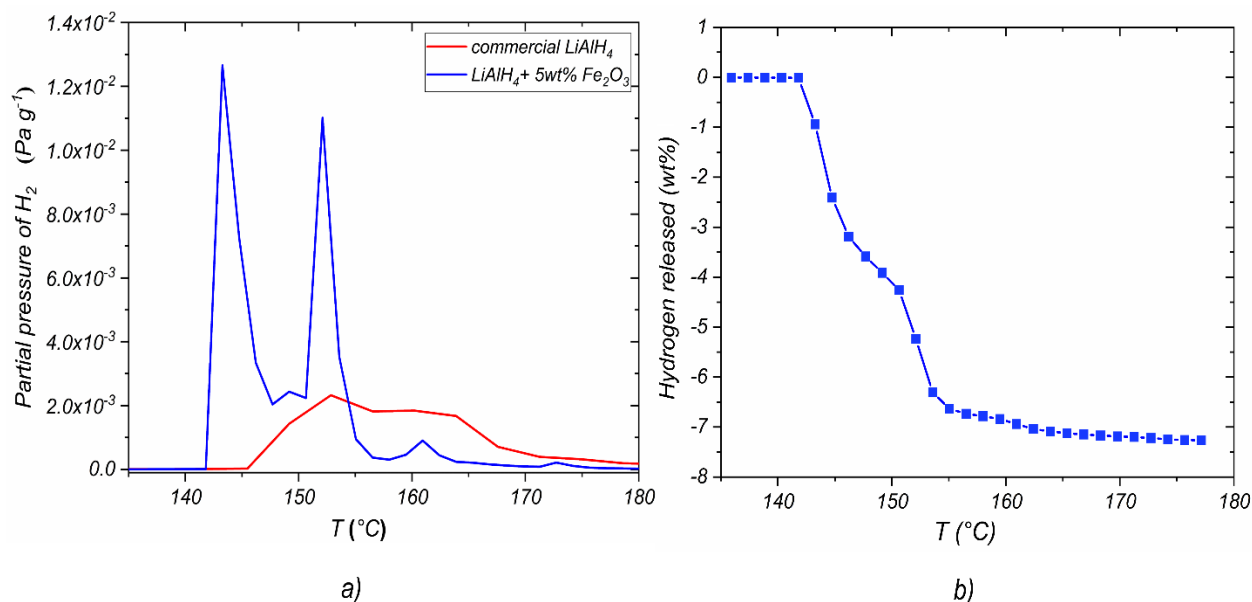

Fig. 1. Temperature dependence of hydrogen partial pressure of temperature in LiAlH$_4$ + 5wt% Fe$_2$O$_3$ milled for 1 minute: a) TPD in temperature range 135°C - 180°C and TPD for the commercial LiAlH$_4$; b) temperature dependence of amount of desorbed hydrogen in LiAlH$_4$ + 5wt% Fe$_2$O$_3$.

Comparing to the commercial LiAlH$_4$ in which hydrogen desorption starts around 153 °C and reaches the second decomposition step at 161 °C, LiAlH$_4$+5wt%Fe$_2$O$_3$ in this study shows a 10 °C lower desorption temperature for both first and second decomposition step, at 143 °C and 152 °C respectively. It is possible that the second decomposition step of commercial LiAlH$_4$ occurs earlier from the previously reported temperature (180 °C - 220 °C) due to the interaction of LiAlH$_4$ with present impurities. The appearance of the peak at low temperatures in LiAlH$_4$ + 5 wt% Fe$_2$O$_3$ as compared to pure LiAlH$_4$, fig.1a, implies the destabilization of the starting and intermediate hydrides that enable faster hydrogen release. The onset of desorption is however not as low as in the samples milled for much longer time (LiAlH$_4$ + 5 wt% Fe$_2$O$_3$ milled for 30 min. starts desorption at 100 °C [3]), demonstrating how longer milling time leads to additional destabilization of the LiAlH4 and can be used for additional tuning of the desorption onset. Our

focus in the investigation is the influence of the dopant, and this is the reason for the selection of the short synthesis time.

The amount of desorbed hydrogen was obtained by integrating the H_2 peak area. Namely, by integrating and normalizing the H_2 partial pressure profile to the mass difference of sample (i.e., the H_2 content) we obtained the dependence of desorbed wt.% H_2 with temperature (fig. 1b). Curve integration shows that $LiAlH_4$ + 5 wt% Fe_2O_3 desorbed approximately 7.3 wt% of hydrogen in the temperature range 143 °C to 180 °C. The amount desorbed in the first decomposition reaction is 4.1 wt% and the second reaction releases 3.2 wt% of hydrogen. The obtained result is consistent with amounts of hydrogen released below 200 °C in previous studies, showing 7.47 wt% [3] for $LiAlH_4$ and 7.5 wt% for Ti-doped $LiAlH_4$ [44]. Also, the sample doped with 5 wt% Fe_2O_3 and milled for 30min released 4.5 wt% and 3.1 wt% of hydrogen in the first and second decomposition step, respectively [3].

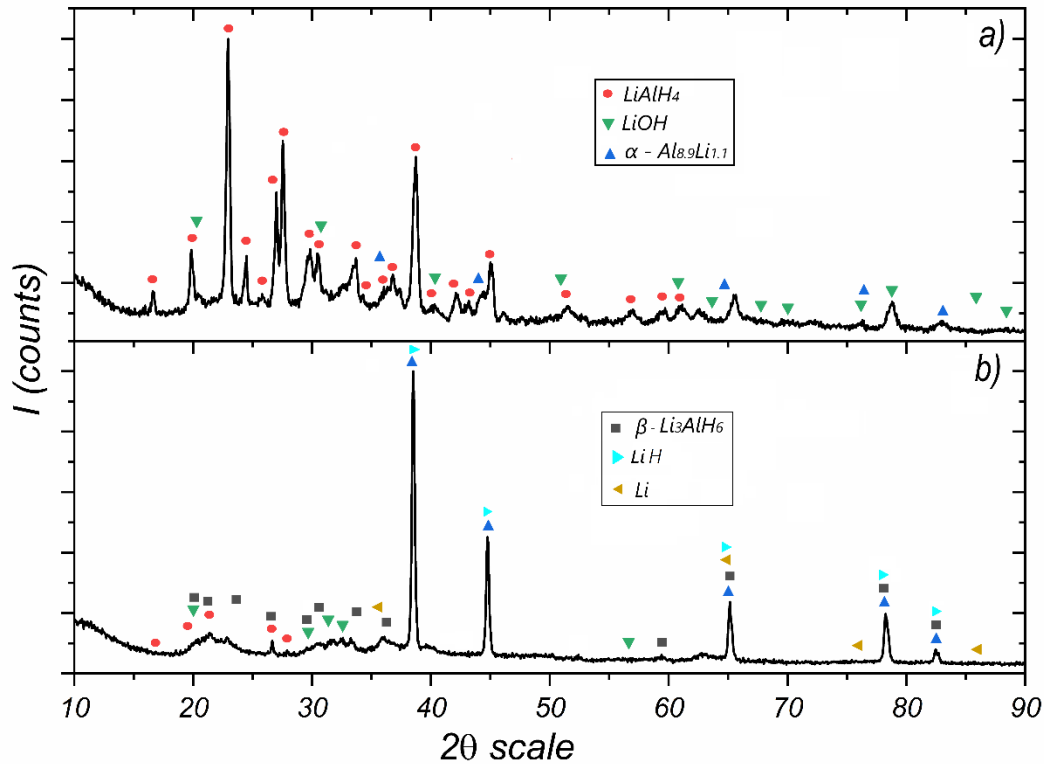XRD spectra of the commercial $LiAlH_4$, before and after desorption are shown in Fig.2.

Fig. 2. XRD patterns of the commercial $LiAlH_4$ a); before b) after hydrogen desorption.

XRD of the commercial $LiAlH_4$ sample (fig. 2a) recorded at ambient conditions shows a dominant phase of $LiAlH_4$. Intermetallic phase α - $Al_{8.9}Li_{1.1}$, present in traces, might be the result of a spontaneous transformation of $[AlH_4]^{2-}$ to $[AlH_6]^{3-}$. In addition, α - $Al_{8.9}Li_{1.1}$, LiOH is also present. The diffraction peaks are shifted towards lower values of the 2θ-scale.

According to the XRD pattern, after desorption (fig. 2b), in the reaction mixture, small amounts of decomposition products β-Li_3AlH_6 and LiH are observed, as well as the intermetallic phase identified as α - $Al_{8.9}Li_{1.1}$. The rest of the components, LiOH, $LiAlH_4$, and weakly crystalized Li, are present in traces.

3.1.2. Local structure and dynamics study

Mossbauer spectroscopy is a technique that allows probing the local structure and the charge state of iron atoms. We use it to see what happens to Fe_2O_3 in different stages of the experiment, in the milling process and during the desorption. ^{57}Fe-Mössbauer spectroscopy due to its high sensitivity as compared to XRD. Recorded spectra and the fit of the $LiAlH_4$+α-Fe_2O_3 sample before and after TPD are presented in Fig.3. The fitted Mössbauer parameters of each subspectrum are presented in Table 1.

Table 1. Room temperature ^{57}Fe-Mössbauer hyperfine parameters for the $LiAlH_4$+α-Fe_2O_3 sample before and after TPD: *A* – relative area of the Mössbauer subspectrum; *CS* – center shift; **<*QS*>** - centroid of quadrupole splitting distribution; $\sigma(QS)$ - standard deviation of quadrupole splitting distribution; ϵ - quadrupole shift in case of combined strong magnetic and weak electric interaction, **<B_{hf}>**– centroid of hyperfine magnetic field distribution, $\sigma(B_{hf})$ - standard deviation of hyperfine magnetic field distribution. The fitting errors are presented in the parenthesis.

Mössbauer subspectrum	A [%]	CS [mms^{-1}]	$<QS> / \epsilon$ [mms^{-1}]	$\sigma(QS)$ [mms^{-1}]	$<B_{\text{hf}}>$ [T]	$\sigma(B_{\text{hf}})$ [T]	iron valence state
Sample before TPD							
QSD site 1	88.80(84)	0.3394(21)	0.7347(34)	0.223(17)	-	-	Fe^{3+}
HFD site 1	11.20(84)	0.385(20)	-0.109(20)	-	49.82(15)	0.57(31)	Fe^{3+}
Sample after TPD							
QSD site 1	19.12(85)	0.363(14)	0.611(18)	0.370(35)	-	-	Fe^{3+}
QSD site 2	3.22(74)	0.717(41)	1.11(12)	0.225(91)	-	-	Fe^{2+}
QSD site 3	1.09(29)	0.609(55)	2.79(13)	0.15(18)	-	-	Fe^{2+}
HFD site 1	48.9(15)	0.0015(15)	-0.0026(14)	-	32.872(11)	0.217(51)	Fe^{0}
HFD site 2	12.11(86)	0.602(18)	-0.030(16)	-	45.04(18)	1.85(21)	$Fe^{2.5+}$
HFD site 3	9.44(70)	0.276(14)	-0.023(12)	-	48.208(95)	0.81(14)	Fe^{3+}
HFD site 4	6.1(17)	-0.064(53)	-0.047(52)	-	28.41(84)	2.76(92)	Fe^{0}

The ^{57}Fe-Mössbauer spectrum of the LiAlH$_4$+α-Fe$_2$O$_3$ sample milled for 1 minute (Fig. 3a) shows the main central doublet, typical for the Fe$_2$O$_3$. This broadened central doublet was fitted with one quadrupole splitting distribution (supplementary, Table 3s, QSD site 1) ascribed to Fe in 3^+ oxidation state according to the center shift value (CS = 0.34 mms^{-1}). This QSD component, with the centroid of quadrupole splitting distribution at <QS> = 0.74 mms^{-1}, has a very similar average quadrupole splitting, as found for the iron (III)-oxide in the superparamagnetic (SPM) state reported by Tuček et al. [45] or for amorphous iron (III)-oxide nanoparticles [46]. The major contribution to this QSD most probably comes from the α-Fe$_2$O$_3$ nanoparticles in the SPM state, with the numerous particles with a large number of surface iron ions and/or presence of defects. We found that the QSD-Mössbauer parameters roughly match the SPM-hematite by Hermanek et al. [47]. Some authors have previously found a much smaller average quadrupole splitting of ~ 0.51-0.56 mms^{-1} for SPM-hematite nanoparticles [48] [49]. It has been found in the case of very small nanoparticles where a large number of surface iron ions has a strong influence on the spectrum, that the nanoparticle's surface iron ions in comparison with the nanoparticle's inner iron ions show enlarged quadrupole splitting [48]. The presence of defects also results in enhanced quadrupole splitting of hematite above the superparamagnetic blocking temperature [49]. There are other smaller contributions, which could be other SPM iron(III)-oxides or iron(III)-hydroxides [50][51][52][53] if they are present in the sample, but the signal is to faint to properly assess what

it due to the overlapping of their possible Mössbauer spectral contributions and the QSD contribution in the spectrum. The six lines absorption feature (sextet) also visible in the spectrum was fitted with one hyperfine magnetic field distribution (Table 1, HFD site 1) and ascribed to the larger hematite nanoparticles due to the distinct Mössbauer parameters of $CS = 0.39$ mms^{-1}, $<Bhf>$ = 50 T and $\epsilon = -0.11$ mms^{-1} which are similar to the bulk α-Fe$_2$O$_3$ [50] [52] [53].

After TPD, the Mössbauer spectrum of the sample is significantly changed (Fig. 3b). The spectrum was fitted with three quadrupole splitting distributions (QSD sites 1-3) and four hyperfine magnetic field distributions (HFD sites 1-4). HFD site 1 was undoubtedly assigned to the α-Fe where Fe is in the zero-valence state (i.e., metallic iron or bcc-Fe), due to the typical metallic iron Mössbauer features, $CS = 0$ mms^{-1}, $<Bhf> \sim 33$ T and $\epsilon \sim 0$ mms^{-1} [52] [53]. For the HFD site 4, the Mössbauer parameters indicated that this phase is magnetically ordered ($<Bhf> \sim$ 28 T) with ^{57}Fe cubic environment due to the quadrupole shift (ϵ) value close to zero. Since the center shift value was also close to zero, this component was ascribed to the bcc-Fe (Al) [54]. According to the distinctive Mössbauer parameters, the HFD sites 2 and 3 belong to the cubic inverse spinel, most likely to the magnetite phase. The stoichiometric magnetite is the cubic inverse spinel and represented by the formula $(Fe^{3+})^A (Fe^{3+} Fe^{2+})^B O^{2-}_4$. The A-sites (tetrahedral sites) are occupied by Fe^{3+} ions and the B-sites (octahedral sites) by the Fe^{3+} and Fe^{2+} ions. At the temperatures above the Verwey transition temperature (~ 119 K for magnetite), the rapid electron exchange exists between the Fe^{2+} and Fe^{3+} ions at the B-sites, and a mixed 2.5^+ iron valence state is detected [55]. The HFD sites 2 and 3 Mössbauer parameters match closely to the ones found for the magnetite phase [52] [53] [55], therefore the HFD site 2 was ascribed to the $Fe^{2.5+}$ B-octahedral site and HFD site 3 to the Fe^{3+} A-tetrahedral site of the cubic inverse spinel. The QSD site 1 has distinct Fe^{3+} character ($CS = 0.36$ mms^{-1}). The signal from nanoparticles is to faint to resolve various possible iron (III)-based phases and iron (III)-oxides/hydroxides contributions to this component. The QSD 2 site and 3 have mixed Fe^{3+} and Fe^{2+} characters according to the CS values of 0.72 mms^{-1} and 0.61 mms^{-1}, respectively. For the QSD site 3, due to the very large quadrupole splitting of $QS = 2.79$ mms^{-1}, the Fe^{2+} character is found as dominant. For the QSD site 2, due to the rather large central shift value, we are also more in favor of more Fe^{2+} character. For each of the spectral contribution, the corresponding spectral areas (Table 1) are exactly proportional to products of the Fe site-specific effective recoil-free fractions and the Fe site-specific occupancies. Under the assumption that all Fe-sites present in the investigated samples have identical effective

recoil-free fractions, the Mössbauer subspectrum areas may be used to quantitatively compare the relative amounts of iron ions on the various types of Fe sites in the samples. In general, these site-specific effective recoil-free fractions are not the same for different Fe sites. For the Fe-bearing phases present in the sample before and after the TPD, we may only give a rough estimate that a significant portion of the iron ions has changed their valence state from Fe^{3+} before TPD to the Fe^{0} and Fe^{2+} after TPD.
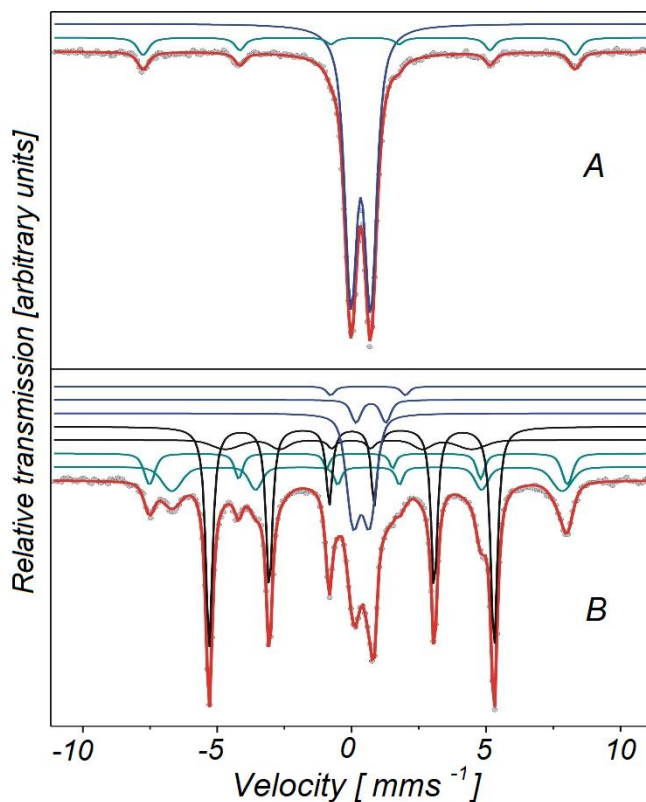

Fig. 3. Room temperature ^{57}Fe-Mössbauer spectra of the $LiAlH_4+\alpha$-Fe_2O_3 sample before (A) and after the TPD procedure (B). Experimental data are presented by the solid circles and the best fit is given by the red solid line. The individual component spectra are shown above the main spectrum fit: A): QSD site 1 (blue doublet), HFD site 1 (green sextet); B): QSD site 1, site 2 and site 3 (blue doublets), HFD site 1 and site 4 (black sextets), HFD site 2 and site 3 (green sextets)

While XRD and Mossbauer spectroscopy provides an insight into the structure and the composition of the system, NMR on the other hand allows us to probe the local dynamics in the system. In $LiAlH_4$, we are interested in checking whether the local motions influence the decomposition process, and how the addition of the catalyst may influence those motions. From

the dynamics point of view, at low temperatures, there are no molecular motions, we can think of all atoms as "frozen" to their positions. Upon heating, the AlH_4 tetrahedra start rotating around different axes. This process is thermally activated. Rising the temperature even higher, those units become detached from the structure, which in turn leads to the decomposition. In related studies of borohydride-based materials, it was possible to extract the activation energies for the rotations of the BH_4 tetrahedra around various axes from the analysis of the temperature dependence of T1 [56] [57]. The onset of motions was also evident from the shape of the proton NMR spectra, which is broad at low temperatures due to the dipolar interactions, and gets narrower upon heating because the motions partially average out those interactions.
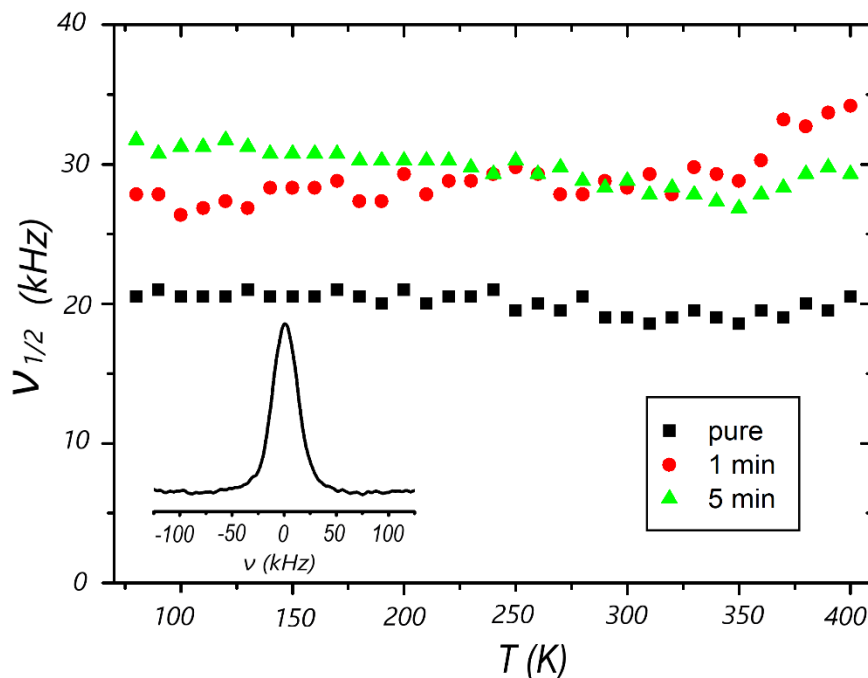

Fig. 4. Proton NMR line width (full width at half maximum) as a function of temperature for three samples. The inset shows the proton spectrum of the 5-min milled sample at 400 K.

In contrast to this ideal picture, it turns out that the presence of Fe_2O_3 smears out most of the effects of the dynamics. Throughout the temperature range, the NMR spectra are broad, and the line shape does not change significantly with temperature. The line has a roughly Gaussian shape, with the full width at half maximum of about 20 kHz for commercial sample and around 30 kHz for the two milled ones. The spin-lattice relaxation temperature dependence for all three samples is also very similar, with T1 being slightly below 100 ms and temperature-independent except for the

higher temperatures (above 350 K), when they get longer. Apparently, the main relaxation mechanism is the coupling of the spins to the paramagnetic centers in the system, introduced by Fe_2O_3 in both milled samples but likely also by some traces of paramagnetic impurities in the pristine $LiAlH_4$ sample as well. Activation energies for rotations of AlH_4 tetrahedra could therefore not be extracted.

3.2. DFT study of LiAlH₄ and Li₃AlH₆

3.2.1. Crystal structure and thermodynamics

Crystal structures of studied Li-alanates are shown in figure 5. Each Li atom in $LiAlH_4$ is surrounded by five AlH_4 tetrahedra (fig. 5a), and it is bound to one hydrogen atom from each of the tetrahedra. Li_3AlH_6 crystal structure (fig. 5b) consists of isolated $[AlH_6]^{3-}$ octahedra connected by six-coordinated Li atoms. Anionic rearrangement (aluminum-tetrahydride anion- slightly distorted tetrahedron transforms to aluminum-hexahydride (octahedral) ionic structure) starts to occur during the ball milling, and later during the decomposition at elevated temperatures.
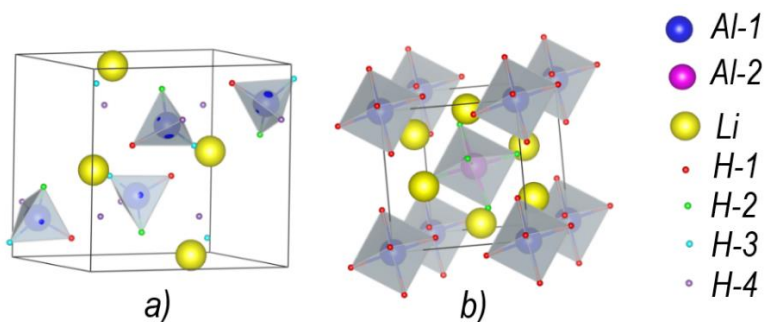

Fig. 5. Crystal structures of a) $LiAlH_4$, polyhedras around Al-1, b) Li_3AlH_6, polyhedras around Al-1 and Al-2

Optimized structural parameters obtained in this study and structural parameters reported previously in literature are presented in table 2.

Table 2. Structural parameters of $LiAlH_4$ and Li_3AlH_6 obtained in DFT calculations (using FPLAPW+lo approach) (at 0 K) and reported experimental values.

| Space group	a (Å)	b (Å)	c (Å)	β (deg)	Optimized atomic positions
LiAlH$_4$ P2$_1$/c	4.780 4.817 [58] 4.845 [32]	7.644 7.802 [58] 7.826 [32]	7.698 7.821 [58] 7.917 [32]	111.5 112.228 [58] 112.50 [32]	Al (0.8985 0.0797 0.2019) Li (0.6925 0.3323 0.4659) H-1 (0.7168 0.1019 0.0990) H-2 (0.8933 0.2037 0.3748) H-3 (0.0587 0.1402 0.0802) H-4 (0.6925 0.4575 0.2609)
Li$_3$AlH$_6$ R-3	7.915 8.113(1) [10] 8.0712 [33]	7.915 8.113(1) [10] 8.0712 [33]	9.313 9.570(1) [10] 9.5130 [33]	91.5 92.07 [10] 86.98 [33]	Al -1 (0.0000 0.0000 0.0000) Al -2 (0.5000 0.5000 0.5000) Li (0.9346 0.4382 0.7501) H-1 (0.2965 0.0741 0.9300) H-2 (0.2035 0.4095 0.5483)

Calculated interatomic distances of Al-H vary between 1.516Å and 1.578Å in LiAlH$_4$ and between 1.730 and 1.734 in Li$_3$AlH$_6$, while the Li-H distance is between 1.882 Å and 2.158Å in LiAlH$_4$ and 1.928Å to 2.043 Å in Li$_3$AlH$_6$ (see table 1s and 2s). Enthalpy of formation of LiAlH$_4$ and Li$_3$AlH$_6$ in reference to the elements in their reference state, and previously reported literature values are presented in supplementary material and are in excellent agreement with earlier reports (supplementary info table 3s).

LiAlH$_4$ is stable at ambient conditions due to the slow kinetics of solid-state transformation to Li$_3$AlH$_6$. However, at higher temperatures, decomposition of LiAlH$_4$ is a three-step process [59]. During the first step, LiAlH$_4$ decomposes to Li$_3$AlH$_6$ and in that process releases 5.3 wt% of molecular hydrogen H$_2$ at temperature range 150°C -175 °C [3] [60], (R1):

$$LiAlH_4 \rightarrow \frac{1}{3} Li_3AlH_6 + \frac{2}{3} Al + H_2 \qquad (R1)$$
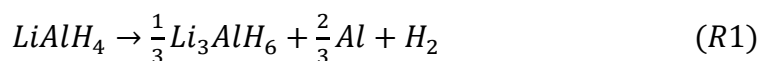
First decomposition reaction is followed by reaction (R2) whereby 2.6 wt% of H$_2$ is released:

$$\frac{1}{3} Li_3AlH_6 \rightarrow LiH + \frac{1}{3} Al + \frac{1}{2} H_2 \qquad (R2)$$
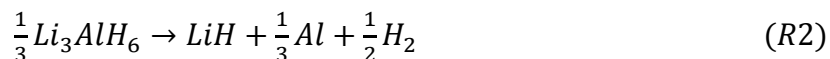
For practical hydrogen storage applications, reactions (R1) and (R2) are achievable, given that they both occur at relatively low temperatures (160°C -210°C) [12].

It has been reported that Ti-doped LiAlH$_4$ [12] shows reversibility under low hydrogen pressure (4MPa).

Above 300°C, LiH and Al form LiAl [61] (2.6 wt% H$_2$).

$$LiH + Al \rightarrow LiAl + \frac{1}{3}H_2 \qquad\qquad (R4)$$

Our calculated desorption energies using the full potential approach are 7.5 kJ/molH$_2$ and 30.4 kJ/molH$_2$, for *R1* and *R2* respectively. The obtained results are in agreement with data calculated at 0K approximation found in the literature [62]. Taking into account that the zero-point energy and temperature effects cancel each other [63], this is a good prediction of the enthalpy and agrees well with the experimental values reported at 298K for LiAlH$_4$ (3.5kJ/molH$_2$) and Li$_3$AlH$_4$ (28.9kJ/molH$_2$) [28]. Literature implies that kinetics can be accelerated by the control of particle size (smaller the particle size - higher the catalytical activity) [64] [65] [6] by increasing for the ratio of surface area to volume, providing numerous nucleation sites, and promoting rapid diffusion of hydrogen [66] or by the use of suitable catalysts [67].

3.2.2 Electronic structure of LiAlH$_4$ and Li$_3$AlH$_6$

When the TBmBJ potential is applied, the valence band (VB) narrows as the electron states are moved toward higher energies as compared to GGA-PBE. Fig. 6 shows the charge density plot for LiAlH$_4$ and Li$_3$AlH$_6$ in both GGA-PBE and TBmBJ approximations, and the results are in agreement with an earlier study on TBmBJ in AlH$_3$ [68].
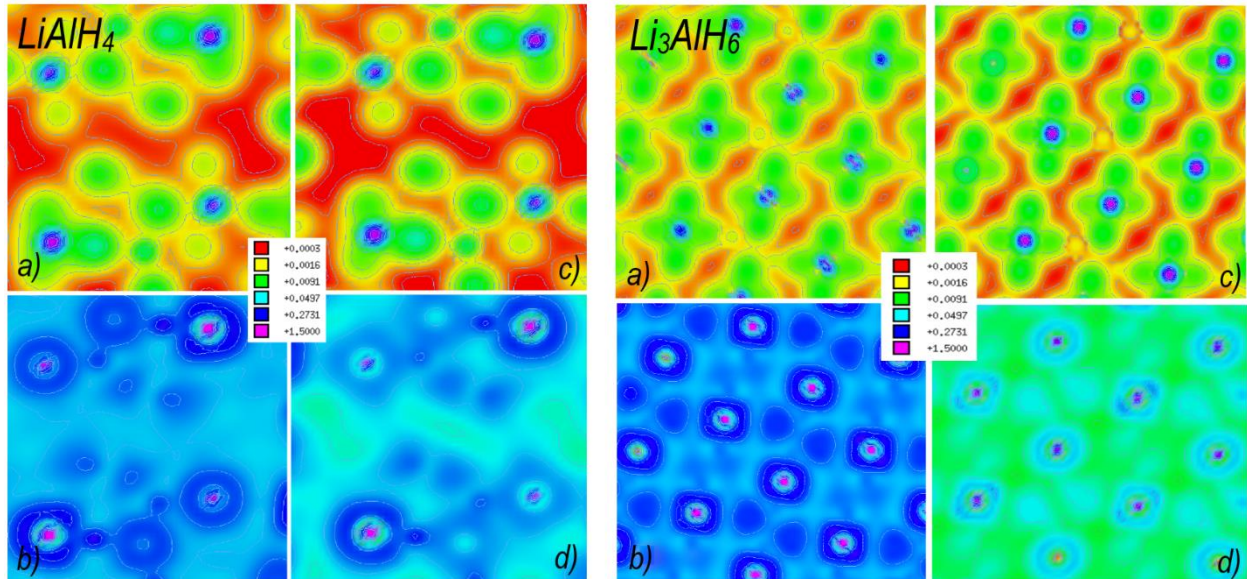

Fig. 6. 2D plots of charge distribution (in e/Å^3) for LiAlH$_4$ and Li$_3$AlH$_6$ in (110) plane. For both hydrides: a) valence band (GGA-PBE), b) conduction band (GGA-PBE), c) valence band (TBmBJ), d) conduction band (TBmBJ).

Places with a high charge density belong to Al and the density decreases in the direction from the center of the nucleus to the atomic periphery. Lithium (yellowish places in the valence zone) appears in places where an accumulation of charge density is observed; this effect is more pronounced in Li_3AlH_6. Given the higher charge density, Al-H ionic bond in $LiAlH_4$ is more distinct comparing to Li-H ionic bond. The bond between Li and AlH_4 in $LiAlH_4$, and between Li and AlH_6 in Li_3AlH_6 is ionic; however, the bond between Al and H in both these compounds shares both covalent and ionic characters, as reported in the literature [69] [70].

Fig. 7 shows the band structure diagrams of $LiAlH_4$ and Li_3AlH_6 obtained using the TBmBJ potential.

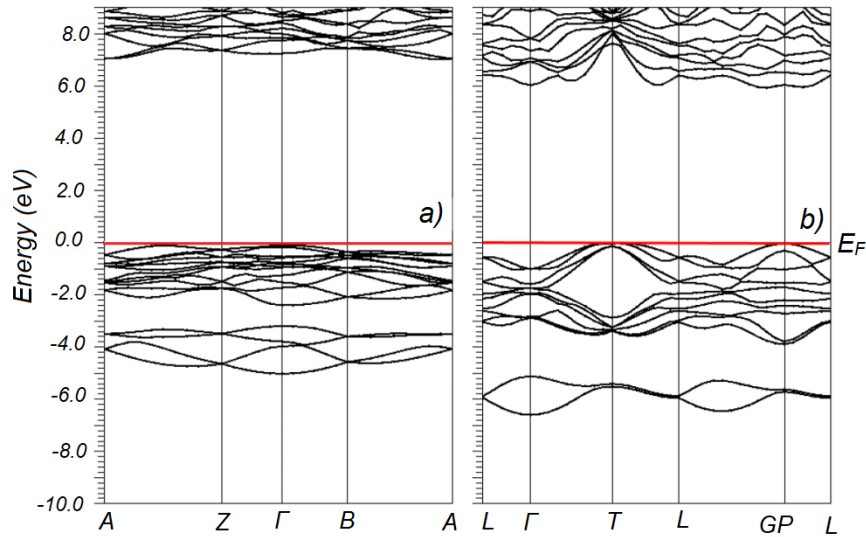Fig. 7. Band structure diagrams for $LiAlH_4$ (a) and Li_3AlH_6 (b) obtained using the TBmBJ potential. Red lines refer to Fermi energy that is set to zero.

The top of the valence band originates from the H-*s* and Al-*p* states (see also Fig. 8) with a dominant contribution of H-*s* states in both compounds. It is observed that studied hydrides are wide band gap materials, with two separated regions in VB. $LiAlH_4$ shows intertwined bands implying localized electrons, compared to Li_3AlH_6 which shows more dispersive bands and probably delocalized electrons [71]. No direct band gap is observed in studied cases. The TBmBJ calculated band gap values of 7.02eV for $LiAlH_4$ and 5.96eV for Li_3AlH_6 are comparable to the literature GW core results (see supplementary info, table 4s). Both hydrides are *p*-type materials. Due to the dominant contribution of hydrogen *s*-states in VB, studied compounds are considered

also as s-hydrides according to S. Zh. Karahzanov et al. classification [72].

Fig. 8 shows the partial density of states for both systems; a difference in the bonding of the inequivalent hydrogen atoms is observed, which is also seen in the calculated cohesive energy (see table 7s). The VB has two regions for both compounds, the lower one corresponding to the Al *s*-states, and the top one to the Al *p*-states.
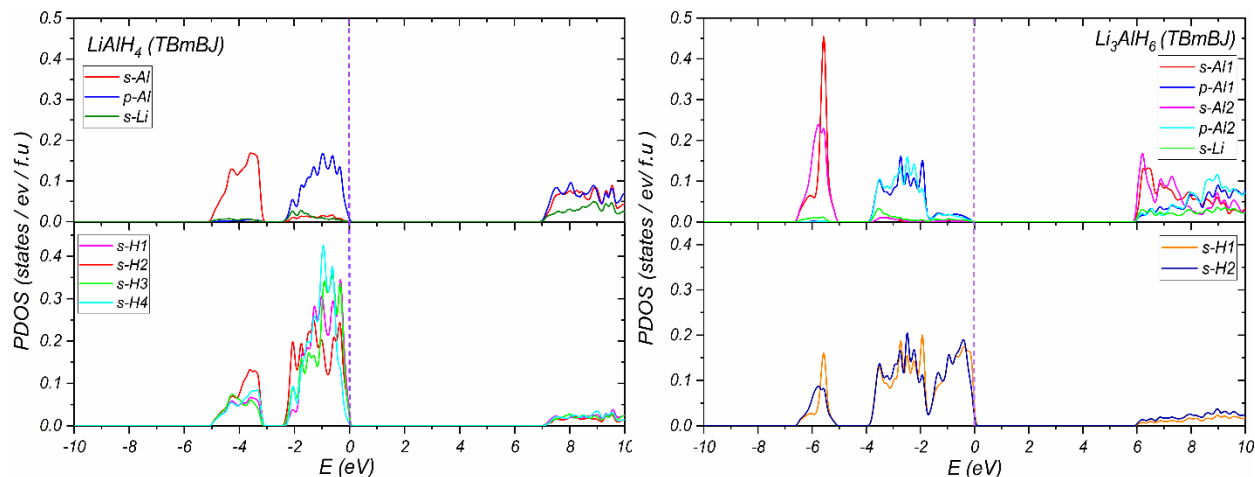

Fig. 8. Orbital-resolved density of states in LiAlH$_4$ and Li$_3$AlH$_6$ obtained using the TBmBJ method

3.2.3. DFT study of destabilization of LiAlH$_4$ and Li$_3$AlH$_6$

Destabilization is proposed as the approach to overcome the obstacles such as slow kinetics and high thermodynamic stability; it can be performed by the implementation of some destabilization technique or doping [73] [74] [75]. Vajo et al. [76] studied alloy formation with Silicon and proved that it causes destabilization of MgH$_2$ and LiH; lowering the dehydrogenation enthalpy for LiH/Si system (120 kJ/mol H$_2$) comparing to unmodified LiH (190 kJ/mol H$_2$).

Based on the experimental study of local structure we observed changes in Fe oxidational number, i.e., transfer of an electron to Fe$_2$O$_3$ during hydrogen desorption. Also, our NMR study showed that paramagnetic centers are present not only in LiAlH$_4$ + 5wt% Fe$_2$O$_3$ but also in the commercial LiAlH$_4$. The presence of impurities in the commercial sample explains the lower desorption temperature obtained in our work as compared to the literature values. To explain the mechanism of influence of transition metal oxides and various impurities in general, and based on the observed charge transfer during hydrogen desorption, we performed additional DFT calculations using the pseudopotential approach.

Destabilization resulting from positive charging of the LiAlH$_4$ and Li$_3$AlH$_6$ is explored by

calculating the energy needed to remove inequivalent hydrogen atoms from the neutral and positively charged cells.

Removing one electron from the studied hydrides destabilizes structure in a way that removal of a hydrogen atom from a charged structure is energetically more favorable, as seen from the cohesive energies calculated for inequivalent hydrogen atoms. This effect is larger in $LiAlH_4$ than in Li_3AlH_6, but interestingly, after charging the unit cells cohesive energy is comparable in both hydrides, ranging from 2.16 to 2.36eV (table 3).

Table 3. Hydrogen cohesive energy (E_{coh}) for the neutral and charged crystal cell of the studied hydrides (taking the energy of isolated hydrogen atom at the theoretical value of 1Ry=13.6 eV).

Compound	Removed atom	E_{coh}(eV)	
		Neutral cell	(+1) charged cell
$LiAlH_4$	H-1	7.08	2.16
	H-2	7.20	2.36
	H-3	7.09	2.22
	H-4	7.18	2.34
Li_3AlH_6	H-1	4.65	2.16
	H-2	4.75	2.20

Figure 9 depicts the amount of cohesive energy needed to remove inequivalent hydrogen atoms from neutral and charged cells of studied hydrides. Removal of the electron from the structure reflected in increased Al-H bond length for all bonds in $LiAlH_4$ by 0.02 to 0.05Å. Results are an indication of the order in which hydrogen is desorbed from these hydrides, but also an implication of the way the thermodynamics of these materials can be tailored in a desirable direction - hydrogen atoms will have looser bonds if destabilization includes charge transfer from the hydrides. Desorption of hydrogen from $LiAlH_4$+5wt%Fe_2O_3 in the narrow temperature interval (fig. 1) indicates similar stability of hydrogen atoms, which is in accordance with calculated cohesive energies of hydrogen atoms in the positively charged cells.

Discussing both experimental and theoretical results obtained, the influence of Fe_2O_3 can be highlighted. In section 3.1.1. we showed that introduction of 5% of Fe_2O_3 during 1min ball-milling of $LiAlH_4$ leads to the significant change in the hydrogen desorption behavior, i.e., the starting

desorption temperature is lowered from 150 °C for LiAlH$_4$, reported in [42], to 143 °C, while the second desorption peak at 153 °C, is significantly lower than 210 °C reported for unmodified LiAlH$_4$. The Mossbauer results presented in section 3.1.2. showed that before TPD iron atoms were found in Fe^{3+} state, while after the desorption valence state is changed (reduced) to Fe^{2+} and Fe^0. During the ball-milling process, particles of dopant are dispersed on the host material in such a way to enable faster dehydrogenation (dopant acts as a catalyst). Based on these main conclusions and DFT results, we can conclude that introduction of Fe$_2$O$_3$ destabilizes LiAlH$_4$ and improves hydrogen desorption performance due to the combined effect of the ball-milling process, leading to thermal activation and existence of surface layer defects, and the effect of charge transfer from LiAlH$_4$ and Li$_3$AlH$_6$ to Fe$_2$O$_3$, leading to weaker bonding of hydrogen atoms.
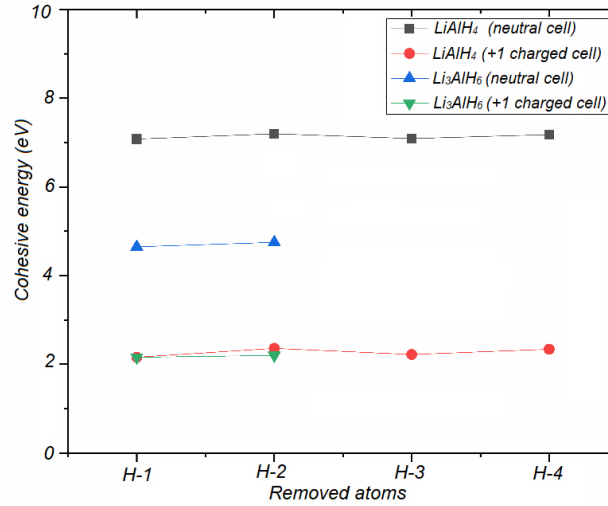

Fig. 9. Cohesive energy needed to remove inequivalent hydrogen atoms from neutral and positively charged crystal cell of studied Li-alanates

4. Conclusion

In the paper, we addressed the electronic structure and thermodynamical properties of a promising hydrogen storage material LiAlH$_4$ and its decomposition product Li$_3$AlH$_6$, as well as the influence of milling with 5 wt% of Fe$_2$O$_3$ on the hydrogen desorption and local structure. Significant improvement of the desorption properties as compared to pure LiAlH$_4$ is seen in LiAlH$_4$+5wt%Fe$_2$O$_3$. Modified sample desorbed 7.3 wt% of hydrogen. First desorption peak in LiAlH$_4$+5wt%Fe$_2$O$_3$ start at 143 °C and second at 154 °C, whereas desorption starts at 150 °C and 210 °C in the pure LiAlH$_4$. The mechanism of this improvement is studied using an experimental and theoretical approach. LiAlH$_4$ destabilization is addressed theoretically by removing hydrogen

atoms for neutral and charged cells and experimentally by ball-milling with a small amount of Fe_2O_3.

^{57}Fe Mössbauer spectroscopy study of ball-milled $LiAlH_4+5wt\%Fe_2O_3$ sample before and after hydrogen desorption revealed significant changes in the iron atom local surroundings. HFD site 1 in a desorbed sample was undoubtedly assigned to the α-Fe where Fe is in the zero-valence state, due to the typical metallic iron Mössbauer features, $CS = 0$ mms^{-1}, $<Bhf> \sim 33$ T and $\epsilon \sim 0$ mms^{-1}. For the HFD site 4, the Mössbauer parameters indicated that this phase is magnetically ordered ($<Bhf> \sim 28$ T) with probably ^{57}Fe cubic environment due to the quadrupole shift (ϵ) value close to zero. For the Fe-bearing phases present in the sample before and after the TPD, we gave a rough estimate that the significant portion of iron ions has changed their valence state from Fe^{3+} before TPD to the Fe^0 and Fe^{2+} after TPD. NMR was used to observe local dynamics in the system. At lower temperatures no molecular motions are seen; upon heating AlH_4 tetrahedra rotations are observed. Paramagnetic centers related to impurities are seen in the commercial sample as well. This change in the valence state of iron during dehydrogenation might be an indicator of charge transfer that leads to the destabilization of both $LiAlH_4$ and Li_3AlH_6, as also shown in DFT calculations. Based on the TBmBJ calculations, both hydrides are classified as a wide band gap materials with calculated band gap energies: 7.02 eV and 5.96 eV for $LiAlH_4$ and Li_3AlH_6 respectively. Also, it is concluded that TBmBJ narrows the valence zone comparing to GGA-PBE. Calculated desorption energies obtained using GGA-PBE are 7.5 kJ/molH$_2$ and 30.4 kJ/molH$_2$ for $LiAlH_4$ and its decomposition product Li_3AlH_6, respectively.

Literature

[1] P. Vajeeston, P. Ravindran, R. Vidya, H. Fjellvåg, A. Kjekshus, Huge-pressure-induced volume collapse in $LiAlH_4$ and its implications to hydrogen storage, Phys Rev. B, 68 (2003) 212101-212104.
[2] R. A. Varin, L. Zbroniec, Mechanical and thermal dehydrogenation of lithium alanate ($LiAlH_4$) and lithium amide ($LiNH_2$) hydride composites, Crystals, 2 (2012) 159-175.

[3] M. Ismail, A. M. Sinin, C. K. Sheng, W. B. Wan Nik, Desorption behaviours of lithium alanate with metal oxide nanopowder additives, Int. J. Electrochem. Sci., 9 (2014) 4959 – 4973.

[4] J. Grbović Novaković, N. Novaković, S. Kurko, S. Milošević Govedarović, T. Pantić, B. Paskaš Mamula, K. Batalović, J. Radaković, J. Rmuš, M. Shelyapina, N. Skryabina, P. de Rango, D. Fruchart, Influence of defects on Mg-based hydrides stability and hydrogen sorption behavior, ChemPhysChem, 20(10) (2019) 1216-1247.

[5] L. H. Kumar, B. Viswanathan, S. S. Murthy, Dehydriding behaviour of LiAlH$_4$-the catalytic role of carbon nanofibers, Int. J. Hydrogen Energ. , 33 (2008) 366-373.

[6] J. Huot, G. Liang, R. Schulz, Mechanically alloyed metal hydride systems, Appl. Phys. A 72 (2001) 187-195.

[7] T.V.S.L. Satyavani, B. Ramya Kiran, V. Rajesh Kumar, A. Srinivas Kumar, S.V. Naidu, Effect of particle size on dc conductivity, activation energy and diffusion coefficient of lithium iron phosphate in Li-ion cells, Engineering Science and Technology, an International Journal 19 (1) (2016) 40-44.

[8] Z. Li, P. Li, Q.Wan, F. Zhai, Z. Liu, K. Zhao, L. Wang, S. Lü, L. Zou, X. Qu, A. A. Volinsky Dehydrogenation improvement of LiAlH$_4$ catalyzed by Fe$_2$O$_3$ and Co$_2$O$_3$ nanoparticles, J. Phys. Chem. C, 117(36) (2013) 18343–18352.

[9] A. Andreasen, T. Vegge, A. S. Pedersen, Dehydrogenation kinetics of as-received and ball-milled, J. Solid State Chem., 178(3) (2005) 3672- 3678.

[10] V.P. Balema, V.K Pecharsky, K.W. Dennis, Solid state phase transformbtions in LiAlH$_4$ during high-energy ball-milling, J. Alloy. Compd., 313 (2000) 69-74.

[11] T. Sun, C.K. Huang, H. Wang, L.X. Sun, M. Zhu, The effect of doping NiCl$_2$ on the dehydrogenation properties of LiAlH$_4$, Int. J. Hydrogen Energ., 33(21) (2008) 6216 – 6221.

[12] J. Chen, N. Kuriyama, Q. Xu, H. T. Takeshita, T. Sakai, Reversible hydrogen storage via titanium-catalyzed LiAlH$_4$ and Li$_3$AlH$_6$, J. Phys. Chem. B 105(45) (2001) 11214 -11220.

[13] Z. Xueping, L. Ping, A. Fuqiang, W. Guoqing, Q. Xuanhui, Effects of Ti and Fe additives on hydrogen release from lithium alanate, Rare Metal Mat. Eng., 37(2008) 400-403.

[14] F. Zhai, P. Li, A. Sun, S. Wu, Q. Wan, W. Zhang, Y. Li, L. Cui, X. Qu, Significantly improved dehydrogenation of LiAlH$_4$ destabilized by MnFe$_2$O$_4$ nanoparticles, J. Phys. Chem. C, 116, (2012) 11939−11945.

[15] Z. Li, P. Li, Q.Wan, F. Zhai, Z. Liu, K. Zhao, L. Wang, S. Lü, L. Zou, X. Qu, A. A. Volinsky Dehydrogenation improvement of LiAlH$_4$ catalyzed by Fe$_2$O$_3$ and Co$_2$O$_3$ nanoparticles, J. Phys. Chem. C, 117(36) (2013) 18343–18352.

[16] A. Andreasen, Effect of Ti-doping on the dehydrogenation kinetic parameters of lithium aluminum hydride, J. Alloy. Compd., 419(1-2) (2006) 40-44.

[17] P. Balema, K. W. Dennisaand, V. K. Pecharsky, Rapid solid-state transformation of tetrahedral [AlH$_4$]$^-$ into octahedral [AlH$_6$]$^{3-}$ in lithium aluminohydride, Chem. Commun., (17) (2000) 1665-1666.

[18] Rafi-ud-din, Q. Xuanhui, L. Ping, L. Zhang, M. Ahmad, Hydrogen sorption improvement of LiAlH$_4$ catalyzed by Nb$_2$O$_5$ and Cr$_2$O$_3$ nanoparticles, J. Phys. Chem. C, Vol. 115 (26) (2011) 13088-13099.

[19] J. L. Wohlwend, P. B. Amama, P. J. Shamberger, V. Varshney, A. K. Roy, T. S. Fisher, Effects of titanium-containing additives on the dehydrogenation properties of LiAlH$_4$: A computational and experimental study, J. Phys.Chem. C, 116 (2012) 22327-22335.

[20] P.B. Amama, J.T. Grant, P.J. Shamberger, A.A. Voevodin, T.S. Fisher, Improved dehydrogenation properties of Ti-doped LiAlH$_4$: Role of Ti precursors.. 2012, J. Phys. Chem. C ,

116, pp. 21886-21894.

[21] M. Ismail, Y. Zhao, X. B. Yu, I. P. Nevirkovets, S. X. Dou, Significantly improved dehydrogenation of LiAlH$_4$ catalysed with TiO$_2$ nanopowder, Int. J. Hydrogen Energ., 36(2011) 8327-8334.

[22] N.N. Mal'tseva, A.I. Golovanova, Decomposition of lithium aluminum hydride in prolonged storage, Russ. J. Appl. Chem., 73 (2000) 747-750.

[23] B.R. Trenhaile, V. N. Antonov, G. J. Xu, K. S. Nakayana, J. H. Weaver, Electron-stimulated desorption from an unexpected source: Internal hot electrons for Br–Si(1 0 0)-(2×1), Surf. Sci.,583(2005) L135-L141.

[24] B. Gergen, H. Nienhaus, W.H. Weinberg, E.W. McFarland, Chemically induced electronic excitations at metal surfaces, Science, 294(5551) (2001) 2521-2523.

[25] H. Nienhaus, B. Gergen, W.H. Weinberg, E.W. McFarland, Detection of chemically induced hot charge carriers with ultrathin metal film Schottky contacts, Surf. Sci., 514 (2002) 172-181.

[26] B. R. Cuenya, H. Nienhaus, E.W. McFarland, Chemically induced charge carrier production and transport in Pd/SiO$_2$/n−Si(111) metal-oxide-semiconductor Schottky diodes, Phys. Rev. B , 70 (2004) 115322-115328.

[27] R. J. Hamers, Bond breaking at surfaces: Electrons or phonons? Surf. Sci., 583 (2005) 1-3.

[28] O. M. Løvvik, S. M. Opalka, H. W. Brinks, B. C. Hauback, Crystal structure and thermodynamic stability of the lithium alanates LiAlH$_4$ and Li$_3$AlH$_6$, Phys. Rev. B, 69 (2004) 134117-134125.

[29] M. J. Van Setten, V. A. Popa, G. A. de Wijs, G. Brocks, Electronic structure and optical properties of lightweight metal hydrides, Phys. Rev. B, 75(3) (2007) 035204 -035216.

[30] D.G. Rancourt, K. Lagarec, Recoil − Mössbauer spectral analysis software for Windows, version 1.0, pp. 43, Ottawa, ON, Canada: Department of Physics, University of Ottawa (1998).

[31] J-Y. Ping, D. G. Rancourt, Voigt-based methods for arbitrary-shape static hyperfine parameter distributions in Mössbauer spectroscopy, Nucl. Instrum. Methods. Phys. Res. B, B58 (1991) 85-97.

[32] N. Sklar, B. Post, The crystal structure of lithium aluminum hydride, Inorg. Chem., 6(4) (1967) 669-671.

[33] H.W. Brinks, B.C. Hauback, The structure of Li$_3$AlD$_6$, J. Alloy. Compd., 354 (2003) 143-147.

[34] P. Giannozzi, S. Baroni, N. Bonini, M. Calandra, R. Car, C. Cavazzoni, D. Ceresoli, G. L Chiarotti, M. Cococcioni, I. Dabo. QUANTUM ESPRESSO: a modular and open-source software project for quantum simulations of materials, J. Phys.-Condens. Mat., 21 (2009) 395502.

[35] P. Blaha, K. Schwarz, G.K.H. Madsen, D. Kvasnicka, J. Luitz, WIEN2k, An augmented plane wave + local orbitals program for calculating crystal properties, Wien: Karlheinz Schwarz, Techn. Universitat Wien, 2001. ISBN 3-9501031-1-2.

[36] P. Hohenberg, W. Kohn, Inhomogeneous electron gas, Phys. Rev., 136(3B) (1964) B864–B871.

[37] J. P. Perdew, Y. Wang, Accurate and simple analytic representation of the electron-gas correlation energy, Phys. Rev. B, 45(23) (1992) 13244-13249.

[38] H.J. Monkhorst, J.D. Pack, Special points for Brillouin-zone integrations, Phys. Rev. B, 13(1976) 5188-5192.

[39] J. P. Perdew, K. Burke, M. Ernzerhof, Generalized gradient approximation made simple, Phys. Rev. Lett., 77 (1996) 3865-3868.

[40] J. Heyd, J. E. Peralta, G. E. Scuseria, R. L. Martin,Energy band gaps and lattice parameters evaluated with the Heyd-Scuseria-Ernzerhof screened hybrid functional, J. Chem. Phys., 123

(2005) 174101-174108.

[41] F. Tran, P. Blaha, Accurate band gaps of semiconductors and insulators with a semilocal exchange-correlation potential, Phys. Rev. Lett. 102(2009) 26401-26404.

[42] C.-P. Hsu, De-hao Jiang, S.-L. Lee, J.-L. Horng, M.-D. Ger, J.-K. Chang, Buckyball-, carbon nanotube-, graphite-, and graphene-enhanced dehydrogenation of lithium aluminum hydride, Chem. Commun., 49(78) (2013) 8845-8847.

[43] N. A. Ali, N. Sazelee, M. S. Yahya, M. Ismail, Influence of K_2NbF_7 Catalyst on the desorption behavior of $LiAlH_4$, Front Chem., 8 (2020) 457- 465.

[44] J. Wang, A. D. Ebner, J. A. Ritter, Physiochemical pathway for cyclic dehydrogenation and rehydrogenation of $LiAlH_4$, J. Am. Chem. Soc., 128 (2006) 5949-5954.

[45] Tuček, Z. Sofer, D. Bouša, M. Pumera, K. Holá, A. Malá, K. Poláková, M. Havrdová, K. Čépe, O. Tomanec, R. Zbořil, Air-stable superparamagnetic metal nanoparticles entrapped in graphene oxide matrix, Nat. Commun., 7 (2016) 12879-12889.

[46] L. Machala, R. Zboril, A. Gedanken, Amorphous iron(III) oxides - A review, J. Phys. Chem. B, 111 (2007) 4003-4018.

[47] M. Hermanek, R. Zboril, I. Medrik, J. Pechousek, C. Gregor, Catalytic efficiency of iron(III) oxides in decomposition of hydrogen peroxide: Competition between the surface area and crystallinity of nanoparticles, J. Am. Chem. Soc., 129 (2007) 10929-10936.

[48] A. M.Van Der Kraan, Mössbauer effect studies of superparamagnetic α-FeOOH and α-Fe_2O_3, Doctoral thesis, TU Delft Repositories (1972).

[49] F. Bødker, M. F. Hansen, C. B. Koch, K. Lefmann, S. Mørup, Magnetic properties of hematite nanoparticles, Phys. Rev. B , 61 (2000) 6826-6838.

[50] M. Krajewski, P.-H. Lee, S.-H. Wu, K. Brzozka, A. Malolepszy, L. Stobinski, M. Tokarczyk, G. Kowalski, D. Wasik, Nanocomposite composed of multiwall carbon nanotubes covered by hematite nanoparticles as anode material for Li-ion batteries, Electrochim. Acta, 228 (2017) 82–90.

[51] Saeed Kamali-M, T. Ericsson, R. Wäppling, Characterization of iron oxide nanoparticles by Mössbauer spectroscopy, Thin Solid Films, 515 (2006) 721 – 723.

[52] M. D. Dyar, D. G. Agresti, M. W. Schaefer, C. A. Grant, E. C. Sklute, Mössbauer spectroscopy of earth and planetary materials, Annu. Rev. Earth Pl. Sc., 34 (2006) 83–125.

[53] J. G. Stevens, A. M. Khasanov, J. W. Miller, H. Pollak, Z. Li [ed.], Mössbauer Mineral Handbook,. Asheville : Mössbauer Effect Data Center, The University of North Carolina, 2005.

[54] E. Jartych, Mössbauer and X-ray diffraction studies of mechanically alloyed Fe-A1, Hyperfine Interact., 99 (1996) 389-399.

[55] B. Kalska-Szostko, D. Satuła, W. Olszewski, Mössbauer spectroscopy studies of the magnetic properties of ferrite nanoparticles, Curr. Appl. Phys., 15 (2015) 226-231.

[56] A. Gradišek, D. B. Ravnsbæk, S. Vrtnik, A. Kocjan, J. Lužnik, T. Apih, T. R. Jensen, A. V. Skripov, J. Dolinšek, NMR study of molecular dynamics in complex metal borohydride $LiZn_2(BH_4)_5$, J. Phys. Chem. C, 117 (2013) 21139–21147.

[57] A. Gradišek, L. H. Jepsen, T. R. Jensen, M. S. Conradi, Nuclear magnetic resonance study of molecular dynamics in ammine metal borohydride $Sr(BH_4)_2(NH_3)_2$, J. Phys. Chem., 120 (2016) 24646–24654.

[58] B. C. Hauback, H. W. Brinks, H. Fjellvåg, Accurate structure of $LiAlD_4$ studied by combined powder neutron and X-ray diffraction, J. Alloy. Compd., 346(1) (2002)184-189.

[59] J. K. Kang, J. Y. Lee, R. P. Muller, W. A. Goddard III, Hydrogen storage in $LiAlH_4$: Predictions of the crystal structures and reaction mechanisms of intermediate phases from quantum mechanics,

J. Chem. Phys., 121(21) (2004) 10623-10633.

[60] J. Block, A. P. Gray, The thermal decomposition of lithium aluminum hydride, Inorg. Chem., 4(3) (1965) 304–305.

[61] P. Vajeeston, P. Ravindran, A. Kjekshus, H. Fjellvåg Structural stability and electronic structure for Li_3AlH_6, Phys. Rev. B, 69 (2004) 020104-020107.

[62] A. R. Akbarzadeh, C. Wolverton, V. Ozolins, First-principles determination of crystal structures, phase stability, and reaction thermodynamics in the Li-Mg-Al-H hydrogen storage system, Phys. Rev. B, 79 (2009) 184102-184111.

[63] K.Batalovic, J.Radakovic, V.Koteski, M.Savic, Density functional theory guide to structure and thermodynamics of metal hydrides – Case study of (Ti, Zr, Hf) Ni intermetallic compounds, Int. J. Hydrogen Energ. 40 (38) (2015) 13029-13038.

[64] M. Arenz, K. J. J. Mayrhofer, V. Stamenkovic, B. B. Blizanac, T. Tomoyuki, P. N. Ross, N. M. Markovic, The effect of the particle size on the kinetics of CO electrooxidation on high surface area Pt catalysts, J. Am. Chem. Soc., 127 (18) 2005 6819–6829.

[65] Study of the activation process of Mg-based hydrogen storage materials modified by graphite and other carbonaceous compounds, S. Bouaricha, J-P. Dodelet, D. Guay, J. Huot, R. Schulz, J. Mater. Res., 16 (10) 2001 2893-2905.

[66] J. Cui, H. Wang, J. Liu, L. Ouyang, Q. Zhang, D. Sun, X. Yao, M. Zhu, Remarkable enhancement in dehydrogenation of MgH_2 by a nano-coating of multi valence Ti-based catalysts, J. Mater. Chem. A, 1 (2013) 5603-5611.

[67] B.Bogdanović, M. Schwickardi, Ti-doped alkali metal aluminium hydrides as potential novel reversible hydrogen storage materials, J. Alloy. Compd., 253-254 (1997) 1-9.

[68] M. Savić, J. Radaković, K. Batalović, Study on electronic properties of α-, β-, γ-AlH_3 − The theoretical approach, Comp. Mater. Sci., 134 (2017) 100-108.

[69] P. Vajeeston, P. Ravindran, A. Kjekshus, and H. Fjellvåg, Reply to "Comment on 'Structural stability and electronic structure for Li3AlH6' ", Phys. Rev. B, 71 (2005) 216102-216105.

[70] P. Ravindran, P. Vajeeston, R. Vidya, H. Fjellvåg, A. Kjekshus, Modeling of hydrogen storage materials by density-functional calculations, J. Power Sources, 159(1) (2006) 88-99.

[71] S.Zh. Karazhanov, P. Ravindran, P. Vajeeston, A.G. Ulyashin, Hydride electronics, Phys. Status Solidi (a) 204 (10) (2007) 3538–3544

[72] S.Zh. Karazhanov, U. Sheripov, A.G. Ulyashin, Classification of hydrides according to features of band structure, Philos. Mag., 89(13) (2009) 1111–1120.

[73] P. Choudhury, S.S. Srinivasan, V.R. Bhethanabotla, Y. Goswami, K. McGrath, E.K. Stefanakos Nano-Ni doped Li-Mn-B-H system as a new hydrogen storage candidate, Int. J. Hydrogen Energ., 34(15) (2009) 6325-6334.

[74] A.W. Vittetoe, M.U. Niemann, S.S. Srinivasan, K. McGrath, A. Kumar, D.Y. Goswami, E.K. Stefanakos, S. Thomas, Destabilization of $LiAlH_4$ by nanocrystalline MgH_2, Int. J. Hydrogen Energ. 34(5) (2009) 2333-2339.

[75] S.V. Alapati, J. K. Johnson, D. S. Sholl, Identification of destabilized metal hydrides for hydrogen storage using first principles calculation, J. Phys. Chem. B, 110 (2006) 8769-8776.

[76] J.J. Vajo, F. Mertens, C.C. Ahn, R.C. Bowman, B. Fultz, Altering hydrogen storage properties by hydride destabilization through alloy formation: LiH and MgH_2 destabilized with Si, J. Phys. Chem. B, 108 (2004) 13977-13983.

[77] P. Claudy, B. Bonnetot, J.M. Letoffe, G. Turck, Determination des constantes thermodynamiques des hydrures simples et complexes de l'Aluminium. IV. enthalpie de formation de LiAIH4 et Li3AIH6, Thermochim. Acta. 27 (1976) 213-227.

[78] T.N. Dymova, D.P. Aleksandrov, V.N. Konoplev, T.A. Silina, A. Sizareva, Spontaneous and thermal decomposition of lithium tetrahydroaluminate LiAlH4: the promoting effect of mechanochemical action on the process, Russ. J. Coord. Chem. 20 (1994) 263-271.

[79] A.Klaveness, H.Fjellvåg, A.Kjekshus, P.Ravindran, O.Swang, A semi-empirical approach to accurate standard enthalpies of formation for solid hydrides, J. Alloy. Compd. 469(1-2) (2009) 617-622.

[80] J. F. Herbst, L. G. Hector, Jr., Energetics of the Li amide/Li imide hydrogen storage reaction, Phys. Rev. B. 72 (2005) 125120-125127.

[81] K. Miwa, N. Ohba, S.-I. Towata, Y. Nakamori, S.-I. Orimo, First-principles study on lithium borohydride LiBH4, Phys. Rev. B 69 (2004) 245120-245127.

[82] C. Wolverton, V. Ozoliņš, M. Asta, Hydrogen in aluminum: First-principles calculations of structure and thermodynamics, Phys. Rev. B 69 (2004) 144109 – 144124.

[83] Y. Fukai, The Metal-Hydrogen System, Springer- Verlag, Berlin (1993) (2nd Edition of Springer Series in Material Science).

[84] T. Ghellab, Z Charifi, H Baaziz, Ş Uğur, G Uğur, F Soyalp, First principles study of hydrogen storage material NaBH4 and LiAlH4 compounds: electronic structure and optical properties, Phys. Scripta 91 (2016) 045804-045821.

[85] O. M. Løvvik, O. Swang, S. M. Opalka, Modeling alkali alanates for hydrogen storage by density-functional band-structure calculations, J. Mater. Res. 20 (12) (2005) 3199-3213.

[86] E.Orgaz, A.Membrillo, R.Castañeda, A.Aburto, Electronic structure of ternary hydrides based on light elements, J. Alloy. Compd. 404-406 (2005) 176-180.